Mon. Not. R. Astron. Soc. **XXX**, XXX–XXX (1999) Printed 15 December 1999 (MN plain TEX macros v1.6)

Development of structure in pores and sunspots: flows around axisymmetric magnetic flux tubes

N.E. Hurlburt[1,2] and A.M. Rucklidge[3,4]

[1] *Lockheed Martin Solar and Astrophysics Laboratory, Organization L9-41 Building 252, Palo Alto, CA 94304, USA*
[2] *email:* hurlburt@lmsal.com
[3] *Department of Applied Mathematics and Theoretical Physics, University of Cambridge, Cambridge CB3 9EW, UK*
[4] *email:* A.M.Rucklidge@damtp.cam.ac.uk http://www.damtp.cam.ac.uk/user/alastair

Received XXX; in original form 1999 June 16

ABSTRACT

Flux elements, pores and sunspots form a family of magnetic features observed at the solar surface. As a first step towards developing a fully nonlinear model of the structure of these features and of the dynamics of their interaction with solar convection, we conduct numerical experiments on idealised axisymmetric flux tubes in a compressible convecting atmosphere in cylindrical boxes of radius up to eight times their depth. We find that the magnetic field strength of the flux tubes is roughly independent of both distance from the centre and the total flux content of the flux tube, but that the angle of inclination from the vertical of the field at the edge of the tube increases with flux content. In all our calculations, fluid motion converges on the flux tube at the surface. The results compare favourably with observations of pores; in contrast, large sunspots lie at the centre of an out-flowing moat cell. We conjecture that there is an inflow hidden beneath the penumbrae of large spots, and that this inflow is responsible for the remarkable longevity of such features.

Key words: Convection – MHD – Sun: interior – Sun: magnetic fields – sunspots.

1 INTRODUCTION

Magnetic fields appear at the surface of the Sun in the form of flux elements, pores and sunspots, though other, more active, stars can have magnetic features covering a significant fraction of their surfaces. This family of magnetic features on the Sun can be parameterized by magnetic flux content. It ranges in scale from flux elements, with diameters down to 100 km (the current limit of resolution), field strengths of 1500 G and magnetic fluxes on the order of 0.001 TWb (10^{17} Mx), through pores, with sizes in the range 2000–4000 km, field strengths of 2000 G and flux contents up to 7 TWb, to sunspots, with diameters up to 50 000 km, field strengths of 3000 G in the umbra and 1500 G in the penumbra, and flux contents varying from 2 to 200 TWb.

The smallest features are formed between the convection cells (granules) on the surface, and have a lifetime of only a few minutes. Magnetic flux accumulates at the corners of supergranules, possibly forming a pore, which grows as it accretes more flux. Occasionally, a pore becomes large enough to develop a penumbra and become a sunspot. Most sunspots are torn apart within a few hours, but the largest sunspots are long-lived, lasting for several weeks, and organise convection around themselves into a moat cell, in which there is a systematic outflow at the surface. The suppression of convective transport by their strong magnetic fields leads to significant reductions in the radiative output of the larger features.

Existing models of the subsurface structure of flux tubes, pores and spots (reviewed by Thomas & Weiss 1992) incorporate balances between pressure and magnetic forces, but do not fully take into account the dynamic and nonlinear nature of the convective atmosphere in which these features live. A sunspot poses particular difficulties because of its filamentary penumbra and complex magnetic field. The most comprehensive magnetostatic model to date is that of Jahn & Schmidt (1994), which incorporates umbral and penumbral regions with thermal properties differing from those of the surrounding convection zone, and with current sheets between the three regions.

In this paper, we present an idealised model of vertical flux tubes in a convecting atmosphere. In order to focus attention on the flux tube and its interaction with convection, we have performed our computations in a cylindrical box (containing a compressible, electrically conducting ideal gas). We have restricted ourselves to axisymmetric solutions in this initial set of calculations. This can be justified as pores and spots can be fairly circular, though in future work we will extend our axisymmetric calculations to the fully three-dimensional case.

In common with earlier work in the Cartesian geometry (Hurlburt & Toomre 1988; Weiss et al. 1990, 1996; Tao

et al. 1998; Blanchflower, Rucklidge & Weiss 1998; Rucklidge et al. 2000), the unstably stratified static reference atmosphere has an initial density stratification, with the density increasing by a factor of eleven over the layer, pressure likewise increasing by a factor of 121, and the ratio ζ of the magnetic to thermal diffusivity increasing from 0.2 to 2.2 with depth. The ratio ζ plays a crucial role in determining the type of convective behaviour seen at onset, with small ζ (less than one) and large magnetic fields favouring oscillatory convection, and large zeta or small fields favouring steady convection. In the photosphere, ζ passes through one at a depth of about 2000 km (Meyer et al. 1974). At that depth, the pressure scale height is on the order of 500 km, so notionally the region of the photosphere being modelled by these calculations from 500 km below the surface and extends to a depth of about 3000 km.

The two- and three-dimensional Cartesian calculations examined patterns of magnetoconvection, both small-scale behaviour found in strongly magnetized regions (Weiss et al. 1990, 1996; Rucklidge et al. 2000), such as the umbrae of sunspots, and large-scale behaviour (Tao et al. 1998), in which magnetic field is expelled from the surrounding convection, as in plage regions. These latter calculations contained many convection cells and magnetic features in a variety of shapes and sizes.

An axisymmetric or cylindrical (or even hexagonal) geometry is better suited to the study of a single magnetic feature, and early incompressible calculations demonstrated that convection readily expels magnetic fields and forms a central flux tube surrounded by a toroidal convection cell (Galloway et al. 1978; Galloway & Moore 1979; Galloway & Proctor 1983). These calculations were carried out in small boxes with the convecting fluid obeying the Boussinesq (incompressibility) assumption, and were extended to case of an inclined outer wall by Watson (1995) and to the mildly compressible case by Cameron (2000).

We combine these two strands of research and solve numerically the partial differential equations governing compressible fluid flow, heat transfer and magnetic induction in an axisymmetric box containing a compressible, electrically conducting ideal gas, with magnetic flux coming up through the box and heat supplied at the lower boundary to drive convection.

Our choice of parameters is guided by our aim to study how the behaviour of magnetic flux tubes in a convecting atmosphere is affected by their flux content. Since the vigour of convection in the unmagnetized parts of the photosphere is unaffected by the presence or otherwise of an adjacent flux tube, we aim to keep the amplitude of convection (as measured by the magnetic Reynolds number, or peak velocity) roughly constant as we increase the flux content. In a box of fixed size, the only way of increasing the flux content is to increase the effective field strength, which has the inevitable effect of suppressing convection. We therefore increase the size of the box along with the flux content to ensure that there is always enough room in the outer, unmagnetized, part of the box to allow convection to proceed relatively unhindered.

The restriction to axisymmetric solutions means that we cannot investigate the fine structure of the penumbrae of sunspots. However, we can examine issues such as the inclination of the magnetic field at the outer edge of the flux tube, which Rucklidge, Schmidt & Weiss (1995) suggested played a role in the transition from pores to sunspots: an inclined outer edge would imply enhanced heating of the outer part of the flux tube and a convectively driven penumbra. To this end, we do not use the vertical magnetic field boundary conditions that have generally been used in the past, but instead match the magnetic field in the box to a current-free (potential) field above the box. This change mainly affects the outer part of the flux tubes by allowing the magnetic field to spread out near the surface. In addition to this, we use a radiative cooling boundary condition based on Stefan's law instead of the usual constant temperature condition.

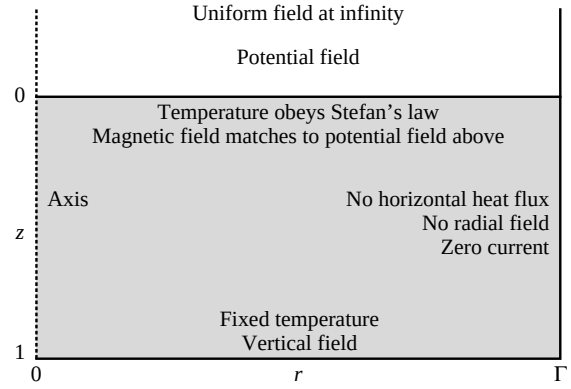

Figure 1. Calculation domain: $0 \leqslant r \leqslant \Gamma$ and $0 \leqslant z \leqslant 1$, indicating the boundary conditions. At $r = 0$ (left edge of the figure), regularity conditions apply. The magnetic field is vertical at the bottom and outer edge of the box, and matches to a potential field at the top. Temperature is fixed at the bottom, and there is no lateral heat flux across the outer edge; the heat flux at the top of the box is determined by Stefan's law. The velocity boundary conditions are stress-free on all edges.

The plan of the paper is as follows. In §2 we give the equations and boundary conditions in appropriate nondimensional form. In §3 we present our results and conclude in §4 with a discussion of the relevance of the results to the magnetohydrodynamics of flux tubes, pores and sunspots. Details of the numerical methods are given in the Appendix.

2 EQUATIONS AND NUMERICAL METHODS

We solve the PDEs that describe compressible magnetoconvection in axisymmetric geometry (see Fig. 1) using a numerical code developed for this purpose. The PDEs are the same as those considered by Hurlburt & Toomre (1988), though we use the form of the PDEs given by Weiss et al. (1996): a layer of electrically conducting gas experiences a uniform gravitational acceleration g directed downwards and possesses a shear viscosity μ, a thermal conductivity K, a magnetic diffusivity η, and a magnetic permeability μ_0, all of which are assumed to be constant. We assume that the fluid satisfies the equation of state for a perfect monatomic gas with constant heat capacities $c_{\rm v}$ and $c_{\rm p} = c_{\rm v} + R_*$, where R_* is the gas constant. The velocity field $\boldsymbol{u}$, magnetic field $\boldsymbol{B}$, temperature T, pressure P and density ρ depend on time t and on the cylindrical coordinates (r, ϕ, z). There is a trivial hydrostatic equilibrium solution with $\boldsymbol{u} = 0$; with an imposed temperature gradient across the layer and a constant thermal diffusion coefficient K, this solution is in the

form of a polytrope, with uniform magnetic field $B_{\rm s}\hat{\boldsymbol{z}}$, and temperature and density having the form

$$T_{\rm s} = T_0(1+\theta z), \qquad \rho_{\rm s} = \rho_0(1+\theta z)^m, \tag{1}$$

where T_0 and ρ_0 are the temperature and density at the top of the layer ($z = 0$ at the top and increases downwards). In addition, m is the polytropic index and θ is the imposed temperature gradient; these two parameters depend on the temperature difference across the layer and are related by $m+1 = gd/R_*\theta T_0$. We work with the dimensionless form of the PDEs, taking the unit of length to be the depth of the layer d and the unit of time to be $d/\sqrt{R_*T_0}$, related to the sound travel time across the layer. This choice of time scale differs by a factor of $\sqrt{T_0/\Delta T}$ from that used by Weiss et al. (1990, 1996), where ΔT is the temperature difference across the layer. We scale the density by ρ_0, the temperature by T_0, and the magnetic field by $B_{\rm s}$. Velocities are scaled by $\sqrt{R_*T_0}$, the sound speed at the top of the layer, and pressure is scaled by $\rho_0 T_0 R_*$.

The equations can be simplified by restricting to axisymmetric solutions. With this assumption, we need only use A, the ϕ component of the vector potential, to represent the magnetic field:

$$\boldsymbol{B} = \left(-\frac{\partial A}{\partial z}, 0, \frac{\partial A}{\partial r} + \frac{A}{r}\right). \tag{2}$$

The nondimensional current density is then only in the ϕ direction:

$$j = (\boldsymbol{\nabla}\times\boldsymbol{B})_\phi = -\nabla^2 A + \frac{A}{r^2}, \tag{3}$$

where

$$\nabla^2 = \frac{\partial^2}{\partial r^2} + \frac{1}{r}\frac{\partial}{\partial r} + \frac{\partial^2}{\partial z^2}. \tag{4}$$

In terms of the nondimensionalised variables, with $\boldsymbol{u} = (u, 0, w)$, the PDEs are then the continuity equation:

$$\frac{\partial\rho}{\partial t} = -u\frac{\partial\rho}{\partial r} - w\frac{\partial\rho}{\partial z} - \rho\boldsymbol{\nabla}\cdot\boldsymbol{u}, \tag{5}$$

where

$$\boldsymbol{\nabla}\cdot\boldsymbol{u} = \frac{u}{r} + \frac{\partial u}{\partial r} + \frac{\partial w}{\partial z}, \tag{6}$$

the two components of the Navier–Stokes equation:

$$\begin{aligned}\frac{\partial u}{\partial t} = &-u\frac{\partial u}{\partial r} - w\frac{\partial u}{\partial z} - \frac{\partial T}{\partial r} - \frac{T}{\rho}\frac{\partial\rho}{\partial r}\\ &- \frac{\sigma\zeta_0\bar{K}^2 Q}{\rho} j\, B_z + \frac{\sigma\bar{K}}{\rho}\left(\nabla^2 u - \frac{u}{r^2} + \tfrac{1}{3}\frac{\partial\boldsymbol{\nabla}\cdot\boldsymbol{u}}{\partial r}\right)\end{aligned} \tag{7}$$

and

$$\begin{aligned}\frac{\partial w}{\partial t} = &-u\frac{\partial w}{\partial r} - w\frac{\partial w}{\partial z} - \frac{\partial T}{\partial z} - \frac{T}{\rho}\frac{\partial\rho}{\partial z} + \theta(m+1)\\ &+ \frac{\sigma\zeta_0\bar{K}^2 Q}{\rho} j\, B_r + \frac{\sigma\bar{K}}{\rho}\left(\nabla^2 w + \tfrac{1}{3}\frac{\partial\boldsymbol{\nabla}\cdot\boldsymbol{u}}{\partial z}\right),\end{aligned} \tag{8}$$

where we have assumed the equation of state for a perfect gas, $P = \rho T$. The dimensionless induction equation is

$$\frac{\partial A}{\partial t} = -uB_z + wB_r - \zeta_0\bar{K}\, j, \tag{9}$$

and the energy equation is (including the viscous and Ohmic heating terms; cf. Landau & Lifshitz 1987)

$$\begin{aligned}\frac{\partial T}{\partial t} = &-u\frac{\partial T}{\partial r} - w\frac{\partial T}{\partial z} - (\gamma-1)T\boldsymbol{\nabla}\cdot\boldsymbol{u} + \frac{\gamma\bar{K}}{\rho}\nabla^2 T\\ &+ \frac{\sigma\bar{K}(\gamma-1)}{\rho}\left(\tfrac{1}{2}\boldsymbol{\tau}:\boldsymbol{\tau} + \zeta_0^2 Q\bar{K}^2\, j^2\right),\end{aligned} \tag{10}$$

where $\boldsymbol{\tau}$ is the rate of strain tensor, defined (in Cartesian coordinates) by

$$\tau_{ij} = \frac{\partial u_i}{\partial x_j} + \frac{\partial u_j}{\partial x_i} - \tfrac{2}{3}\delta_{ij}\boldsymbol{\nabla}\cdot\boldsymbol{u}. \tag{11}$$

In cylindrical coordinates, we find that

$$\begin{aligned}\tfrac{1}{2}\boldsymbol{\tau}:\boldsymbol{\tau} = &\left(\frac{\partial u}{\partial z} - \frac{\partial w}{\partial r}\right)^2 + \tfrac{4}{3}(\boldsymbol{\nabla}\cdot\boldsymbol{u})^2\\ &+ 4\left(\frac{\partial u}{\partial z}\frac{\partial w}{\partial r} - \frac{u}{r}\frac{\partial w}{\partial z} - \frac{u}{r}\frac{\partial u}{\partial r} - \frac{\partial u}{\partial r}\frac{\partial w}{\partial z}\right)\end{aligned} \tag{12}$$

(cf. Chandrasekhar 1961).

The dimensionless quantities that have appeared in the PDEs are: θ, the initial temperature gradient, m, the polytropic index, γ, the ratio of specific heats, σ, the Prandtl number, $\bar{K}$, the dimensionless thermal conductivity:

$$\gamma = c_{\rm p}/c_{\rm v}, \qquad \sigma = \mu c_{\rm p}/K, \qquad \bar{K} = \frac{K}{(R_*T_0)^{1/2}\rho_0 d\, c_{\rm p}}, \tag{13}$$

ζ_0, the magnetic diffusivity ratio at the top of the layer, and Q, the Chandrasekhar number:

$$\zeta_0 = \eta\rho_0 c_{\rm p}/K \qquad \text{and} \qquad Q = \frac{B_{\rm s}^2 d^2}{\mu_0\mu\eta}. \tag{14}$$

These seven dimensionless parameters define our problem, along with one additional geometric parameter, Γ, the scaled radius of the computational domain.

In addition to these, there are secondary dimensionless parameters, defined here for convenience. We use the mid-layer Rayleigh number R to measure the importance of buoyancy forces compared to viscous forces:

$$R = \theta^2(m+1)\big(1-(m+1)(\gamma-1)/\gamma\big)\frac{(1+\theta/2)^{2m-1}}{\sigma\bar{K}^2}, \tag{15}$$

and the total vertical magnetic flux Φ is used to compare experiments done with different values of Q:

$$\Phi = 2\sqrt{Q}\int_0^\Gamma r B_z\, dr = \sqrt{Q}\Gamma^2, \tag{16}$$

where an inessential factor of π has been removed. We also define the local plasma beta, the ratio of pressure to magnetic pressure:

$$\beta = \frac{2\rho T}{\sigma\zeta_0\bar{K}^2 Q|\boldsymbol{B}|^2}, \tag{17}$$

and the magnetic Reynolds number:

$$R_{\rm m} = \frac{\max|\boldsymbol{u}|}{\zeta_0\bar{K}} \approx 100\max|\boldsymbol{u}| \tag{18}$$

for the choice of parameters made in §3. Finally, we mention that the local sound speed is $\sqrt{\gamma T}$ and the local Alfvén speed is $|B|/\sqrt{\mu_0\rho}$. We note that the magnetic diffusivity ($\zeta_0\bar{K}$) is constant, while the thermal diffusivity $\gamma\bar{K}/\rho$ depends on density and hence on position.

2.1 Boundary conditions

Our computational domain is a cylinder of radius Γ, so (r, z) satisfy

$$0 \leqslant r \leqslant \Gamma, \qquad 0 \leqslant z \leqslant 1, \tag{19}$$

with $z = 0$ at the top of the box (see Fig. 1). We require that all variables be sufficiently well behaved at the axis ($r = 0$) that the differential operators in the PDEs are non-singular. This implies that

$$\frac{\partial \rho}{\partial r} = u = \frac{\partial w}{\partial r} = A = B_r = \frac{\partial B_z}{\partial r} = j = \frac{\partial T}{\partial r} = 0 \tag{20}$$

at $r = 0$. Terms like u/r are evaluated using l'Hôpital's rule, while terms like u/r^2 are found to cancel with other terms.

At the bottom and sides of the box, we use the boundary conditions that have been widely used in the Cartesian version of this problem. At $z = 1$, these are constant temperature, vertical magnetic field, impenetrable and stress-free:

$$T = 1 + \theta, \qquad \frac{\partial A}{\partial z} = w = \frac{\partial u}{\partial z} = 0. \tag{21}$$

At $r = \Gamma$, we have no lateral heat flux across the slippery, perfectly conducting side wall:

$$A = \frac{\Gamma}{2}, \qquad \frac{\partial T}{\partial r} = u = \frac{\partial w}{\partial r} = j = 0. \tag{22}$$

This value of A is chosen so that the initial vertical uniform field satisfies $B_z = 1$.

However, on the top surface, we diverge from the standard practice (constant temperature and vertical magnetic field conditions), and apply instead a radiative, potential field condition. Specifically, we set

$$\frac{\partial T}{\partial z} = \theta T^4, \qquad \frac{\partial A}{\partial z} = \mathcal{M}_{\rm pot}(A), \qquad \frac{\partial u}{\partial z} = w = 0, \tag{23}$$

where $\mathcal{M}_{\rm pot}(A)$ is a linear operator described below. Similar conditions have been used by Hurlburt, Matthews & Proctor (1996) and Blanchflower et al. (1998) in Cartesian geometry, though the potential field condition is harder to impose in cylindrical coordinates.

For the potential field upper boundary condition, we require that the magnetic field in the domain matches (that is, the values of B_r and B_z are continuous across the boundary, or equivalently, A and $\partial A/\partial z$ are continuous across the boundary) a current-free field given by the flux function $A_{\rm pot}$, where

$$\nabla^2 A_{\rm pot} - \frac{A_{\rm pot}}{r^2} = 0. \tag{24}$$

This equation can be solved in general by a linear combination of Bessel functions of r multiplied by exponential functions of z. It is possible to solve the equation in the entire semi-infinite region $z < 0$, but we have found that this leads to the magnetic field having a sharp corner as it leaves the domain at $r = \Gamma$. Instead, we suppose that there is an infinitely tall conducting cylinder of radius Γ above the domain, and that the magnetic field becomes uniform as $z \to -\infty$. Such a potential field can be written as:

$$A_{\rm pot}(r, z) = \tfrac{1}{2} r + \sum_{i=1}^{\infty} \hat{A}_i J_1(\lambda_i r/\Gamma) e^{\lambda_i z/\Gamma}, \tag{25}$$

where the $\hat{A}_i$ are constants, J_1 is the first-order Bessel function and the λ_i are the positive roots of the equation

$$J_1(\lambda) = 0. \tag{26}$$

The constants $\hat{A}_i$ can be computed from the values of $A(r, 0) = A_{\rm pot}(r, 0)$ at the top of the domain:

$$\hat{A}_i = \frac{2}{\Gamma^2 J_2^2(\lambda_i)} \int_0^{\Gamma} r(A(r, 0) - \tfrac{1}{2} r) J_1(\lambda_i r/\Gamma)\, dr, \tag{27}$$

and from these, the value of the vertical derivative of A can be computed at $z = 0$:

$$\frac{\partial A}{\partial z} = \sum_{i=1}^{\infty} \frac{\lambda_i}{\Gamma} \hat{A}_i J_1(\lambda_i r/\Gamma) \equiv \mathcal{M}_{\rm pot}(A). \tag{28}$$

In practice, we truncate the sums at $n_r - 2$, where n_r is the number of grid point in the r direction. We compute the coefficients $\hat{A}_i$ by setting $z = 0$ in (25) and inverting the resulting matrix equation, rather than by computing integrals, as in (27). Since the boundary condition is linear, the value of $\partial A/\partial z$ at each grid point along the top boundary is a linear combination of the values of A at those grid points; the matrix corresponding to the operator $\mathcal{M}_{\rm pot}$ can be computed in advance.

The density does not in principle satisfy boundary conditions, but we impose the value of the normal derivative of ρ obtained from the momentum equations (7) and (8) in order to ensure that these are consistent with the boundary conditions.

2.2 Numerics

We use a code specifically developed for these calculations; details of the numerical method are given in the Appendix. We achieve sixth-order spatial accuracy using compact finite differences (Lele 1992) and fourth-order temporal accuracy using a modified (explicit) Bulirsch–Stoer technique for integrating forward in time. At the boundaries, the first-order derivatives are evaluated to fifth order accuracy, and the second-order derivatives are fourth-order accurate. The calculations were initiated with a relatively low numerical resolution (40 grid intervals in the vertical), then the resolution was increased until the solution had been properly resolved. The grid intervals were chosen to be equal in the two directions. The timestep was limited by the Courant condition, multiplied by a safety factor of 0.3.

3 NUMERICAL EXPERIMENTS

With eight dimensionless parameters to control the system, of necessity we limit ourselves to varying two of these: the radius of the cylinder Γ and the Chandrasekhar number Q. The other parameters are fixed at the well-used values of $\gamma = 5/3$, $\sigma = 1$, $\zeta_0 = 0.2$, $m = 1$, $\theta = 10$ and $\bar{K} = 0.0489898$, which give a mid-later Rayleigh number of $R = 100\,000$. With this choice, the basic atmosphere is well stratified, with the density and temperature increasing by a factor of eleven over the layer, and with enough thermal forcing to drive reasonably vigorous convection in the absence of a magnetic field.

The effective ratio of magnetic to thermal diffusivities, $\zeta_0 \rho$, also varies by a factor of eleven over the layer, from 0.2

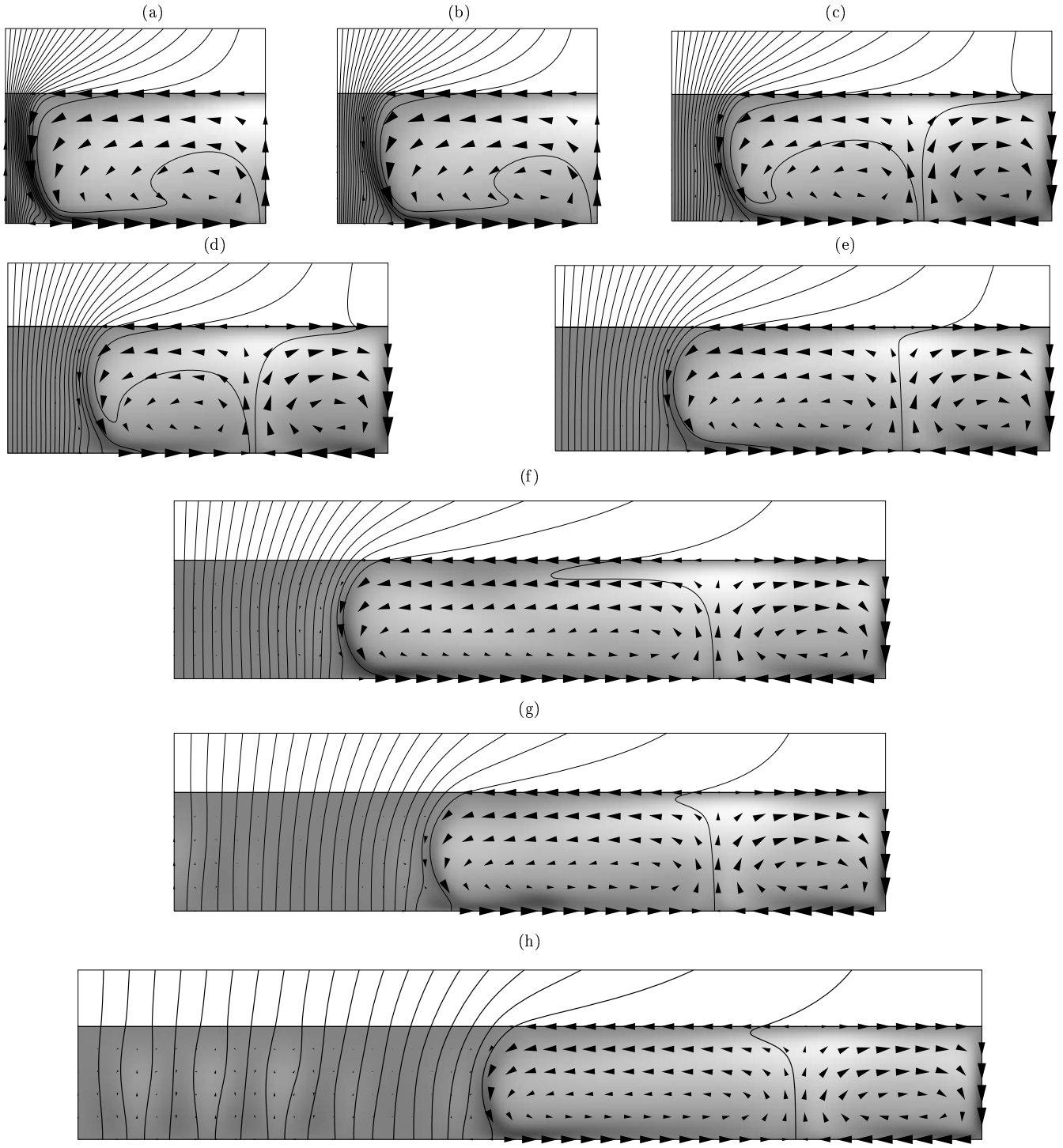

Figure 2. Single and two roll steady flux tubes: the magnetic flux increases by a factor of 2 from frame to frame. The parameters are: $\gamma = 5/3$, $\sigma = 1$, $\zeta_0 = 0.2$, $m = 1$, $\theta = 10$, $R = 100\,000$, with aspect ratios and Chandrasekhar numbers (a) $\Gamma = 2$, $Q = 5.0625$; (b) $\Gamma = 2$, $Q = 20.25$; (c) $\Gamma = 3$, $Q = 16$; (d) $\Gamma = 3$, $Q = 64$; (e) $\Gamma = 4$, $Q = 81$; (f) $\Gamma = 6$, $Q = 64$; (g) $\Gamma = 6$, $Q = 256$. (h) $\Gamma = 8$, $Q = 324$. Each frame shows (in the lower portion) magnetic field lines in black, velocity pointers in black and temperature deviation from the initial temperature gradient in grey-scale (light signifying hot, dark signifying cold, and mid-grey signifying the unperturbed temperature gradient). The upper portion shows the potential magnetic field above the layer. The field line contour levels are chosen such that a uniform magnetic field would have uniformly spaced field lines. The area of the velocity pointers is proportional to the magnitude of the velocity. The horizontal coordinate is r, with the axis on the left; the vertical coordinate is z, increasing downwards.

Table 1. Properties of flux tubes as functions of flux content Φ and box radius Γ.

Φ	Γ	Q	$n_r \times n_z$	$R_{\rm m}$	$r_{\rm max}$	$\alpha_{\rm max}$	r_{10}	α_{10}	$r_{\rm mid}$
6.4	1.5	8.0	241×161	220.0	0.09	16.7	0.54	80.8	0.24
9.0	1.5	16.0	241×161	202.4	0.16	23.1	0.64	80.7	0.29
6.4	2.0	2.5	361×181	272.4	0.09	17.2	0.52	81.3	0.24
9.0	2.0	5.1	241×121	257.8	0.14	21.6	0.62	82.0	0.28
12.7	2.0	10.1	241×121	240.6	0.21	27.0	0.74	82.1	0.32
18.0	2.0	20.3	241×121	223.1	0.28	28.8	0.89	82.3	0.38
25.5	2.0	40.5	241×121	204.6	0.37	32.8	1.05	82.8	0.45
36.0	3.0	16.0	241×81	241.3	0.43	35.8	1.19	83.2	0.50
50.9	3.0	32.0	241×81	239.7	0.54	37.4	1.40	82.2	0.60
72.0	3.0	64.0	241×81	233.6	0.69	40.8	1.65	81.8	0.73
101.8	3.0	128.0	241×81	223.9	0.88	42.9	1.90	79.9	0.90
144.0	3.0	256.0	241×81	212.9	1.11	45.9	2.14	76.8	1.12
101.8	4.0	40.5	361×91	253.3	0.83	44.5	1.94	83.9	0.84
144.0	4.0	81.0	361×91	249.1	1.04	45.6	2.29	83.4	1.03
203.6	4.0	162.0	361×91	239.4	1.31	48.1	2.63	81.5	1.28
288.0	4.0	324.0	361×91	228.8	1.66	49.4	2.97	76.6	1.61
288.0	6.0	64.0	481×81	262.2	1.58	50.7	3.30	84.3	1.54
407.3	6.0	128.0	481×81	264.7	1.90	51.0	3.72	84.1	1.85
576.0	6.0	256.0	481×81	256.7	2.33	49.7	4.14	80.2	2.26
814.6	6.0	512.0	481×81	238.1	2.95	52.7	4.71	75.4	2.86
814.6	8.0	162.0	641×81	247.6	3.11	51.8	5.36	78.6	3.03
1152.0	8.0	324.0	641×81	237.8	3.80	52.1	6.03	72.0	3.71
1629.2	8.0	648.0	641×81	220.2	4.59	51.2	6.71	65.1	4.49

at the top to 2.2 at the bottom in the initial static state. Linear theory predicts that convection will set in as overstable oscillations if this ratio is smaller than one and if Q is large enough, otherwise the initial form of convection is steady (Chandrasekhar 1961; Cattaneo 1984a,b; Weiss et al. 1990). With our choice of parameters, convection is suppressed if Q exceeds about 4000. The initial instability as Q is decreased from this value appears to be a Hopf bifurcation leading to weakly oscillating convection, but for lower values of Q, this solution is quickly replaced by a state in which the convection sweeps the majority of the magnetic flux to the centre of the box (see Fig. 2). We will concentrate on this last class of solutions, in which the magnetic flux is well separated from the convection.

3.1 Varying flux content

We use the total magnetic flux, Φ, as the main controlling parameter, and aim to show how this parameter determines the properties of flux tubes. To this end, we start with a relatively small value of the flux and increase it by factors of $\sqrt{2}$, in different sized boxes. In order to ensure that the properties of the flux tubes are as far as possible independent of the size of the box, Γ, we have computed solutions with various values of Γ, from $\Gamma = 1.5$ to $\Gamma = 8$ (see Fig. 2 and Table 1). We used two criteria to determine the box size: first, we required that there should be sufficient room in the unmagnetized part of the box that convection (as measured by the magnetic Reynolds number) should not be inhibited by the presence of the flux tube. In particular, we aimed to keep $R_{\rm m}$ in the range 200–270. Second, the box should be large enough that the amount of magnetic field at the outer boundary should be insignificant, so that we could be sure that the properties of the flux tube are not influenced by the outer boundary. The properties of these flux tubes are summarised in Table 1.

In each calculation, we started either from a small perturbation of the trivial solution or from a previously calculated state, and integrated the PDEs until the final state was achieved (often several hundred dimensionless time units). In most cases, the final state is steady, though in the larger boxes, there are oscillations around a basically steady state. In the smallest flux tubes ($\Phi < 10$), the flux tube is partially evacuated, with a minimum density about one tenth of its initial value; the number of grid points required to resolve this density minimum (which occurs on the axis in the smallest tubes but at the outer edge on the top in the larger tubes) limited our exploration of the smallest flux tubes.

In a typical calculation, the magnetic field collects into the centre of the region, forming a vertical flux tube in which convection is almost entirely suppressed, while convection carries on in the outer, unmagnetised, regions. With $\Gamma \leqslant 2$ (Fig. 2a,b), there is only one roll in the box, but there is room for two rolls in larger boxes. With $\Gamma = 3$ (Fig. 2c,d), the upwards plume between the two rolls occurs at a radius of about 2, indicating that $\Gamma = 2$ is in fact sufficient for the lower values of Φ. For larger Φ, the flux tube grows and the rising plume is pushed outwards. In the largest tubes (Fig. 2h), there is weak convection in the magnetized region.

Near the axis, the magnetic field strength is sufficiently large that it can suppress or even eliminate convective motions, so the temperature in these inner regions is unperturbed from the static temperature gradient with the temperature close to 1 at the surface. In the innermost parts of the flux tubes, the magnetic field strength is almost uniform (the field line contours are evenly spaced), but the field

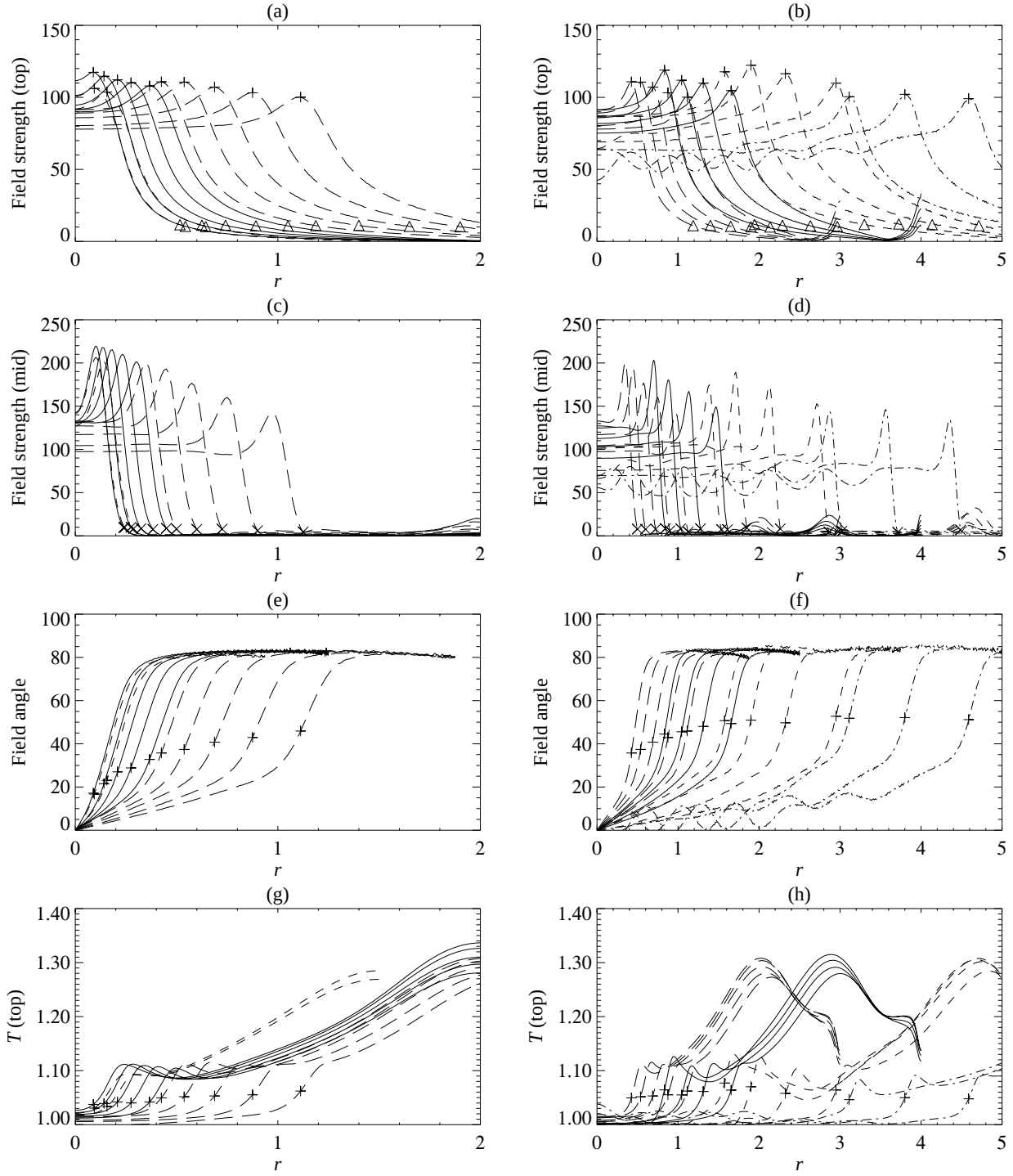

Figure 3. Properties of the family of flux tubes, as a function of radius. (a,b) The field strength $\sqrt{Q}|B|$ at the top of the layer; (c,d) field strength at the middle of the layer ($z = 0.5$). (e,f) angle of the magnetic field at the top of the layer (in degrees, measured from the vertical); (g,h) temperature at the top of the layer. The panels on the left are for $\Gamma = 1.5$ (short dashes), $\Gamma = 2.0$ (solid) and $\Gamma = 3.0$ (long dashes), while the panels on the right are for $\Gamma = 3.0$ (long dashes), $\Gamma = 4.0$ (solid) and $\Gamma = 6.0$ (short dashes), $\Gamma = 8.0$ (dash-dot), The plus symbols (+) denote $r_{\rm max}$; the triangles ($\triangle$) denote r_{10}; and the crosses ($\times$) denote $r_{\rm mid}$. Note that some of the calculations have the same value of flux but different values of Γ, so some of the curves overlap.

strength increases towards the outer edge of the tube before dropping off to negligible values outside the tube. The increased field strength is also associated with a weak counter-eddy within the flux tube and a narrow (width about 0.1 units) current sheet bounding the flux tube. The potential field boundary conditions mean that the field spreads out as it goes up to the surface, and expands to fill the region above the fluid, and so becomes increasingly inclined towards the

edge of each flux tube. The size of the flux tubes increases with the total flux content Φ such that the field strength in the tube is almost independent of its size, as is the width of the current sheet. The region of greatest field strength also has the strongest (field-aligned) downflows, with correspondingly lower temperatures. The temperature at the surface in the flux tube is almost uniform, and about 30% lower than the peak temperature outside the flux tube. The angle at which the field is inclined to the vertical at the edge of the tube increases with the size of the tube, ranging from 15–20° in the smallest tubes to 50–55° in the largest. The minimum of the plasma β occurs near the outer edge of the flux tube, where the density is lowest and the field strength is highest, and is in the range 0.1–0.2, apart from the smallest ($\beta_{\min} = 0.05$) and largest ($\beta_{\min} = 0.25$) flux tubes. But the most striking feature that all solutions share is that the flow always converges on the flux tube at the surface.

In Fig. 3, we show some of the properties of this family of flux tubes, plotted against radius r. These graphs show the runs described in Table 1. From Fig. 3(a,b), we note that the field strength in the inner part of the flux tube is almost independent of flux and of radius (it varies by less than a factor of two over two orders of magnitude of Φ), and that the position of the peak field strength moves outwards as the flux increases. The field strength $|B|$ has been multiplied by a factor of $\sqrt{Q}$ in order to make the actual units of field strength the same in all plots. Similarly, at a depth $z = 0.5$ in Fig. 3(c,d), the flux tube has a relatively uniform interior with field strength roughly independent of flux and of radius, surrounded by a region of stronger magnetic field, which drops rapidly to zero outside the flux tube. The oscillation in field strength in Fig. 3(b,d) in the largest boxes is caused by convection in the magnetized region. In Fig. 3(e,f), we plot the angle of the magnetic field to the vertical at the top of the layer: the field starts vertical at the axis with an inclination that increases, slowly at first, then rapidly becomes nearly horizontal outside the flux tube. Finally, in Fig. 3(g,h), we see that the temperature at the top of the layer is near its unperturbed value ($T = 1$) in the inner part of the flux tube; there is a local temperature maximum near the edge, but the temperature reaches its real maximum of about 1.3 above the rising hot plume.

There are a number of ways that the sizes of these flux tubes could be measured. We have chosen three measurements of radius, which are $r_{\max}$, the radius at which the field strength is at its maximum value at the top of the layer, r_{10}, the radius at which the field strength is 10% of its maximum value at the top of the layer, and r_{mid}, the radius at which the field strength is 10% of its maximum value at the level $z = 0.5$. Similarly, we define $\alpha_{\max}$ and α_{10} to be the angle that the field makes with the vertical at $r = r_{\max}$ and $r = r_{10}$. The locations $r = r_{\max}$, r_{10} and r_{mid} are indicated by plus symbols (+), triangles (△) and crosses (×) respectively in Fig. 3. The radii r_{10} and r_{mid} contain 85–95% of the total magnetic flux in all cases.

The three radii of the flux tubes are plotted against total magnetic flux Φ in Fig. 4(a): the radii increase roughly as $\sqrt{\Phi}$. This behaviour would be expected if the field strength $\sqrt{Q}|B|$ were independent of Φ. This expectation is verified at the midpoint of the layer in Fig. 4(b), and at the top of the layer if the flux tube radius is taken to be r_{10}. However, the radii $r_{\max}$ measured at the top of the layer diverge from the constant mean field expectation for the lower values of magnetic flux. One reason for this is that for lower fluxes, there is not enough room within the flux tube for the counter-eddy that concentrates the field near the edge, and so the peak field moves on to the axis. In the kinematic limit, the peak field is indeed on the axis, and the size of the tube is determined by the diffusivity of the magnetic field (the radius goes as $R_{\mathrm{m}}^{-1/2}$) rather than by the flux content (Weiss 1966). However, in our calculations, the stratification of the basic atmosphere is strong enough that the flux tube is evacuated before we achieve the weak field limit (cf. Cattaneo 1984a).

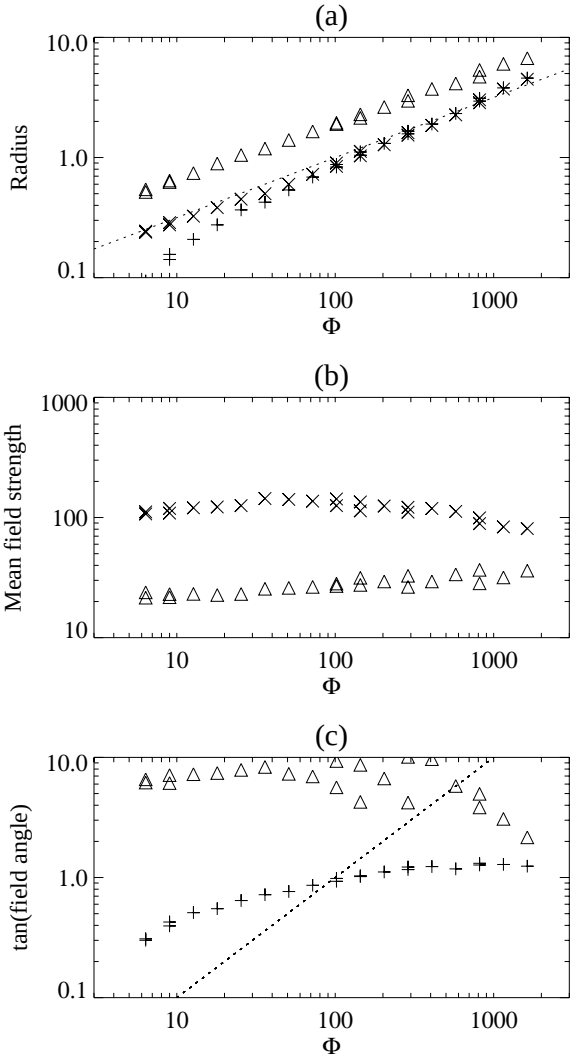

Figure 4. Properties of the family of flux tubes, as a function of magnetic flux. (a) The radii of the flux tube at the top of the layer: pluses (+) denote $r_{\max}$ triangles (△) denote r_{10} and crosses (×) denote r_{mid}. The dotted line indicates the relationship that we would expect if the field strength were independent of magnetic flux: the radius would be proportional to $\sqrt{\Phi}$. (b) Mean field strength: Φ/r_{10}^2 (△) and Φ/r_{mid}^2 (×). (c) Tangent of the field angle at $r = r_{10}$ (△) and at $r = r_{\max}$ (+). Note that the inclination of the field to the vertical at $r_{\max}$ increases with magnetic flux. The dotted line in (c) is $\log\tan\alpha_{\max}$ proportional to $\log\Phi$ (cf. Leka & Skumanich 1998).

Finally, in Fig. 4(c), we show the angle of the magnetic field $\alpha_{\max}$ and α_{10} at the top of the layer and at $r = r_{\max}$ and $r = r_{10}$. The field is almost horizontal (75–85°) at $r = r_{10}$, independent of flux, but the angle of the field at $r = r_{\max}$ increases with magnetic flux from 15–20° in the smallest tubes, levelling off at 50–55° for the larger tubes. This systematic increase of field angle at $r = r_{\max}$ is not obvious in Fig. 2, where the peak field at the outer edge of the tube is not readily apparent, but is clear in Fig. 3(e,f).

In the very largest flux tubes, weak convection can establish itself in the inner part of the tube (cf. Fig. 2h). This convection inevitably takes the form of travelling waves (owing to the asymmetry between the axis and edge of the tube). These waves have triangular shape, as also observed in Cartesian geometry (Hurlburt et al. 1989), and slowly travel inwards. Similar inward travelling waves have also been seen in incompressible axisymmetric convection (Tuckerman & Barkley 1988). The convection rolls travel inwards in this case, but both directions of travel have been observed in two-dimensional Cartesian calculations with imposed oblique magnetic fields (Matthews et al. 1992; Hurlburt et al. 1996).

3.2 Direction of the flow

As mentioned above, one striking feature of these solutions is that the fluid flow always converges on the flux tube at the top of the layer, and the tube is surrounded by a pronounced down-draft. This strong preference appears to be a consequence of the compressibility of the gas: in an incompressible fluid modelled using the Boussinesq assumption, the problem has a reflection symmetry in the horizontal midplane, so there can be no preference for flows of either direction. This symmetry is also broken by the use of different temperature and magnetic field boundary conditions at the top and bottom of the layer, though in a weakly stratified layer, we have found solutions with both orientations.

We have attempted to find solutions that have the flow diverging from the tube at the surface, trying different initial conditions or artificially reversing the flow. In all cases, after a (possibly lengthy) transient the system settles down to a state in which the flow converges on the the flux tube at the top, though sometimes a two-roll solution is replaced by a one-roll solution. When this happens, the properties of the flux tube (radius and field inclination) in the two cases only differ by a small amount. Only in the cases of the smallest boxes ($\Gamma \leqslant 2$) did a systematic outflow occur, but this was associated but a concentration of magnetic field near the outer edge, and the flow reverted to its more usual orientation in somewhat larger boxes.

Fig. 5 shows part of a transient for $\Gamma = 6$ and $Q = 256$. At one stage in the calculation (Fig. 5a), the fluid is moving away from the flux tube at the surface, and the flow near the tube is dominated by a strong down-draft. This down-flow is rapidly carried away from the tube (Fig. 5b,c), taking some magnetic field with it. The hot, partly magnetized material just outside the flux tube develops a thermal instability and another cold down-draft develops (Fig. 5d). This one is carried towards the flux tube (Fig. 5e,f), and an inflow is established around the flux tube, eventually settling down to Fig. 2(g). Other parameter values show similar behaviour: whenever the flow diverges from the flux tube at the top, it drags out the field, and the convection roll adjacent to the tube develops a series of cold down-drafts. These continue until one of them is pushed into the tube (as in Fig. 5f), at which point the flow settles down to a (relatively) steady inflow. The thermal instability at the top of the upward moving plume appears to be enhanced if the plume is partly magnetized. This instability arises because of buoyancy braking (cf. Hurlburt, Toomre & Massaguer 1984; Steffen, Ludwig & Krüss 1989; Spruit, Nordlund & Title 1990; Rast 1995), when heat losses exceed heat supply at the centre of the upflow. The instability has also been seen in two-dimensional Cartesian calculations with the potential and radiative thermal boundary conditions (Blanchflower et al. 1998).

3.3 Varying magnetic boundary conditions

In Fig. 6, we compare two calculations done at the same parameter values ($\Gamma = 3.0$ and $Q = 64$), but with potential magnetic and radiative temperature boundary conditions in Fig. 6(a), and vertical magnetic and fixed temperature boundary conditions in Fig. 6(b). Apart from the flux tube being slightly more concentrated at the surface with vertical field boundary conditions, while the magnetic field spreads out at the top with potential magnetic boundary conditions, there is little qualitative difference between the two. Blanchflower et al. (1998) carried out a systematic comparison between the two sets of boundary conditions in two-dimensional convection and came to the same conclusion.

3.4 Varying magnetic Reynolds number

The mechanism responsible for determining the size and field strength of the flux tubes in these calculations can be investigated by considering the effect of varying the magnetic Reynolds number $R_{\rm m}$. In Fig. 7, we show the results of calculations done with $\Gamma = 3.0$ and $Q = 64$, with ζ_0 varying from 0.05 to 0.56 in factors of $\sqrt{2}$. Once the final solution has been achieved, this has the effect of varying $R_{\rm m}$ from 60 to 1000. With larger $R_{\rm m}$ (smaller ζ_0), the current sheet at the outer edge of the flux tube becomes narrower, and the tube itself becomes smaller with higher field strengths. Higher numerical resolution is needed for the smaller values of ζ_0, not only to resolve the narrower current sheets, but also to cope with reductions in the density in the narrow regions of peak field strength near the edge of the tube. For the smallest values of ζ_0, the density drops to less than a tenth of its initial value.

The dotted lines in Fig. 7 indicate that the field strength goes roughly as $R_{\rm m}^{1/2}$ and the tube radius goes as $R_{\rm m}^{-1/4}$. These scaling laws are consistent with the laws obtained by Galloway et al. (1978), who found for incompressible axisymmetric magnetoconvection that the peak field strength went as $(R_{\rm m}/\log R_{\rm m})^{1/2}$. We have not done sufficient computation to detect the weak logarithmic dependence. In this compressible configuration, the field strength cannot continue to grow as $R_{\rm m}$ is increased once the flux tube is appreciably evacuated.

4 DISCUSSION

In summary, the main features of the computed family of flux tubes are: convection is suppressed inside the flux tube;

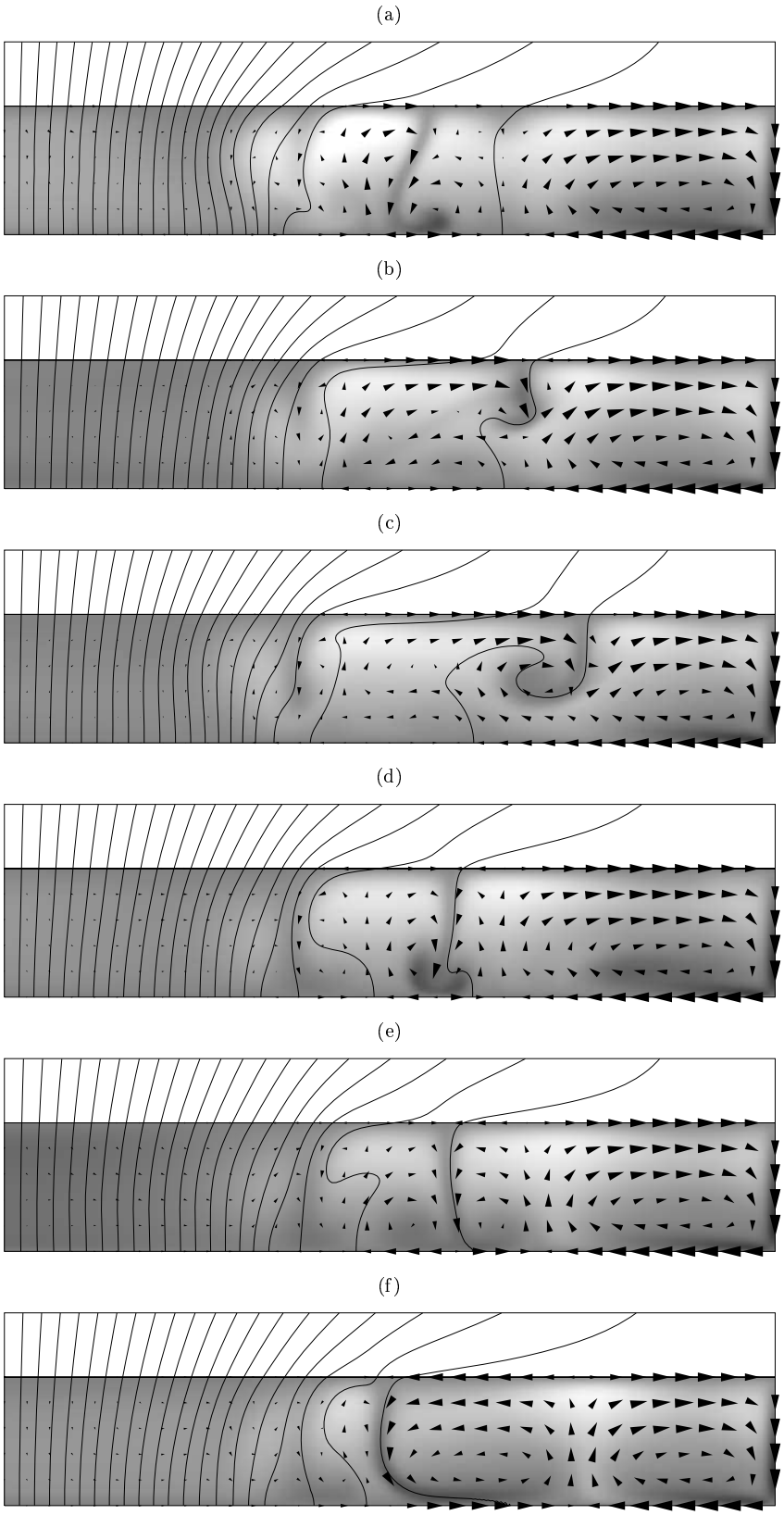

Figure 5. Transient solution, with $\Gamma = 6$, $Q = 256$. Starting from frame (a), the dimensionless times are (b) $t = 1.1$, (c) $t = 2.1$, (d) $t = 5.7$, (e) $t = 7.1$, and (f) $t = 11.8$. The system finally settles down to a steady state (Fig. 2g) after 120 time units.

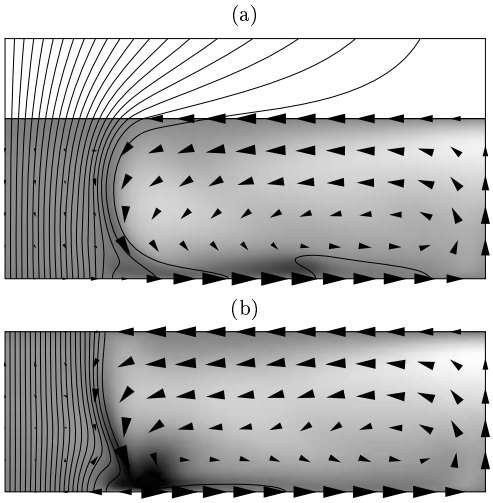

Figure 6. Comparing (a) potential field and radiative temperature with (b) vertical field and fixed temperature boundary conditions, with $\Gamma = 3.0$ and $Q = 64$ (see Fig. 2d).

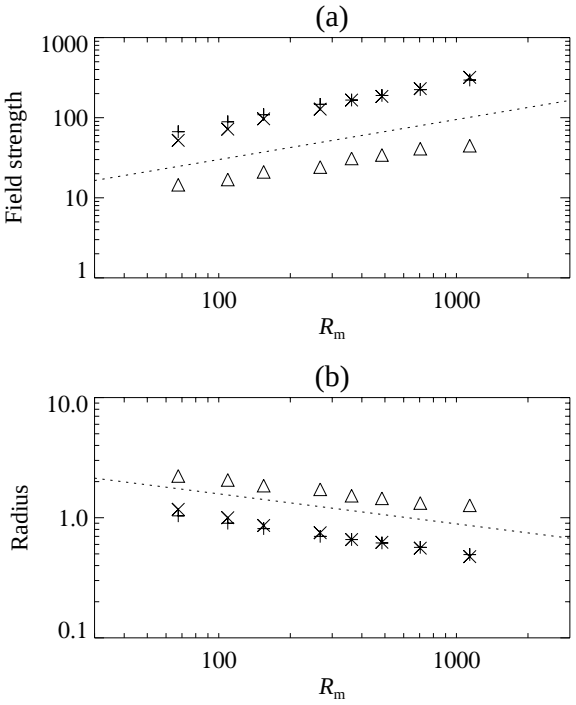

Figure 7. (a) Field strength and (b) flux tube radius as functions of R_m, with $\Gamma = 3.0$ and $Q = 64$, and $0.05 \leqslant \zeta_0 \leqslant 5.6$. The dotted lines are (a) $R_m^{1/2}$ and (b) $R_m^{-1/4}$. Triangles, crosses and plusses have the same meaning as in Fig. 3.

there is a uniform temperature and field strength inside the tube; there is a temperature contrast of about 30% between the inside and the outside of the tube; the field strength is independent of flux content and so the size of the tube increases with flux content; the field angle increases with flux content and size; and the flow always eventually converges on the flux tube at the surface. In the largest flux tubes, there is weak convection that takes the form of inwardly travelling waves.

These properties are in remarkably good agreement with the observed features of pores. Sütterlin, Thim & Schröter (1994) measured the field strength in a single pore of diameter 5000 km and found it to vary only a few percent from its mean value of 2000 G, dropping sharply to low values beyond the edge of the pore. Skumanich (1999) reported observations of 51 pores with a nearly universal vertical field component of 800 ± 32 G, independent of the size of the pore. The angle of inclination during the evolution (growth) of a pore also increases systematically with pore size (Leka & Skumanich 1998). We find that $\log \tan \alpha_{\max}$ is proportional to $\log \Phi$; Leka & Skumanich (1998) found a similar linear relation but with a larger slope (cf. Fig. 4c). Keil et al. (1999) reported annular regions of convergence and downflow around pores. Sobotka et al. (1999a) determined that within about 1500 km of the edge of a pore, flows are dominated by inward motions, while at greater distances, granules move away from pores.

The preference in the calculations for flows converging on the flux tube at the surface was pronounced, and we did not find any persistent states with diverging flows (though such flows were often seen as transients, as in Fig. 5). Indeed, pores are usually seen at the centre of converging flows at the granular and supergranular scales, but large, long-lived sunspots are surrounded by their persistent outflowing moat.

In compressible convection calculations, the flow appears to be driven primarily by concentrated cold downdrafts, with more gently rising extended up-drafts (cf. Hurlburt et al. 1984, Stein & Nordlund 1989, 1998; Spruit et al. 1990; Spruit 1997; Nordlund & Stein 1997; Steiner et al. 1998). The cooler conditions at the surface near a flux tube provide a natural source of cold material, leading to downflows around the tube and hence inflows. Parker (1979) envisaged these inflows would occur at a depth of about 1000 km. However, his model does not account for the presence of the outflowing moat. Meyer et al. (1974) suggested that the flow should converge on a sunspot at a depth of 12 000 km, rise up the side of the outwardly sloping tube and diverge at the surface in a manner consistent with the transport of momentum in cavities with sloping walls (cf. Watson 1995). We have seen here that such a flow would evolve rapidly as magnetic field is ripped from the flux tube.

Flows around pores can be therefore explained as an inflow at the surface associated with cold downflows at the edge of the pore (see Fig. 8a). The situation with sunspots is more complicated. All our calculations indicate that there should be inflows and downflows around long-lived sunspots, driven by the cool temperatures associated with suppressed convection, and indeed helioseismic observations (Duvall et al. 1996) suggest that there are systematic downflows beneath active regions. On the other hand, large sunspots lie at the centre of an out-flowing moat cell.

We therefore propose that the domain covered by our calculations is relevant to flows at some depth (the darker region in Fig. 8b) below optical depth unity, the level at which the moat flow is observed. If the lid of the box is notionally raised (the lighter region in Fig. 8b) to allow for this, the inward and downward super-granular flow could be hidden beneath the outer inclined edge of a large flux tube. Meanwhile, the surrounding counter-cell would provide the outflowing moat at the surface. While they are suggestive, our calculations are unable to produce this configuration

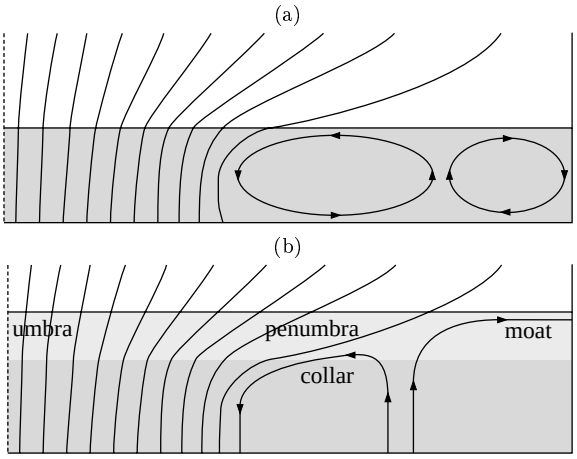

Figure 8. Schematic depictions of (a) the calculations and the flows around a pore, and (b) the conjectured flow around a sunspot.

directly because there is not enough room under the inclined edge of the flux tube to accommodate a convection cell (we would need a much deeper layer to achieve this), nor do we have an optically thick atmosphere above our convecting layer.

This conjectured arrangement of the flows around the flux tube combines features of the models of Meyer et al. (1974) and Parker (1979). It provides the inflowing collar that would confine magnetic field at a depth somewhat below the surface, and the upflow that is needed to provide the material for the moat. The pattern of flow is only established after a long transient, suggesting that only a few spots would achieve this arrangement, and the stability of the flow could account for the remarkable longevity of spots with moats. The upflow below the inclined outer edge could also provide heat for a convective instability leading to the formation of a filamentary penumbra (Jahn & Schmidt 1994; Rucklidge et al. 1995).

The conjecture is supported by two indirect observations as well as the helioseismic measurements of Duvall et al. (1996). First, bright features (called grains) in the penumbra travel inwards if they start in the inner two-thirds of the penumbra, otherwise they travel outwards (Sobotka, Brandt & Simon 1999b). However, these features may all be associated with outwards material motion (cf. Schlichenmaier, Jahn & Schmidt 1998). Second, Rast et al. (1999) have observed systematic bright rings around twelve isolated sunspots, with a 10K increase in temperature within one sunspot radius of the penumbra, and suggested this might be due either to sunspots being relatively shallow phenomena, or to flows near a sunspot being more effective at transporting heat. The second explanation appears to be the most likely given the presence of organised moat flows around sunspots, and our calculations suggest the form that these flows might take beneath the surface.

The next stages of the calculations will address the linear stability of these axisymmetric flux tubes, then follow with the fully nonaxisymmetric nonlinear development of any instabilities. Preliminary non-axisymmetric results are presented by Hurlburt, Matthews & Rucklidge (2000). We will also explore more realistic magnetic boundary conditions, connecting the flow to force-free fields above (cf. Martens et al. 1996; Neukirch & Martens 1998) and to coronal heating models (Alexander, Hurlburt & Rucklidge 2000). Even in the axisymmetric geometry, the presence of of twisted fields could be included (Jones & Galloway 1993): twisted tubes are likely to be seen as untwisted tubes do not rise through the convection zone unscathed (Hughes, Falle & Joarder 1998). Large long-lived sunspots do not have significant azimuthal magnetic fields, so it would be interesting to explore whether the presence of twisted fields alter the stability of the flux tube. In nonaxisymmetric geometry, instabilities are likely to occur both in the outer convecting regions, where the torus-shaped convection cell will break up into smaller cells (Hurlburt et al. 2000), and in the flux tube itself. The travelling waves seen in the inner part of the largest flux tubes may be related to umbral dots (cf. Weiss et al. 1990), which do travel inwards (Sobotka, Brandt & Simon 1997). The outer parts of the flux tube are liable to both fluting instabilities (Parker 1975), which are stabilized by buoyancy (Meyer, Schmidt & Weiss 1977), and to convective instabilities (cf. Rucklidge et al. 1995, Schlichenmaier & Schmidt 1999); linear (Matthews et al. 1992) and nonlinear (Julien, Knobloch & Tobias 2000) theories suggest that there should be an abrupt switch from three-dimensional convection to two-dimensional radially aligned convective rolls as the angle of the field to the vertical is increased.

A combination of more realistic boundary conditions and three-dimensional geometry will be needed to explain the complex flows and field geometries associated with the penumbra and the Evershed effect. Even in simple sunspots, the inclination of the magnetic field varies by 30° between the light and dark filaments of the penumbra, with the field in the dark filaments being nearly horizontal at the edge of the spot (Title et al. 1993). The outward Evershed flow appears to take place above the dark penumbral filaments (Shine et al. 1994), and extends beyond the white light boundary of the sunspot (Rimmele 1995a,b). The arched flux tubes associated with these flows originate within the sunspot and can return to the surface outside or even with the penumbra (Stanchfield et al. 1997; Westendorp Plaza et al. 1997; Schlichenmaier & Schmidt 1999).

Despite the importance of sunspots and their magnetic fields, we are still far from understanding them in detail. Recent observations with modern CCD and image restoration techniques are yielding significant improvements in our empirical understanding, with ever-increasing levels of complexity. Even simple features of pores and sunspots have proved a challenge to explain theoretically, and complex fluted magnetic field geometries, on scales near the observation limits, will be even more difficult.

ACKNOWLEDGMENTS

We are grateful to N.O. Weiss for his valuable input and suggestions at all stages of this project. We would like to thank C.A. Jones, E. Knobloch, A. Skumanich, A.M. Title and J. Toomre for scientific discussions, N. Brummell, F. Cattaneo, R. Hollerbach, S.K. Lele, J. Leorat, P.C. Matthews, M.R.E. Proctor, L.S. Tuckerman for helpful conversations and their comments on numerical techniques, and T. Bernstam, J. Cheng and A. Min for keeping NEH busy. This work was supported in part by NASA contract NAG5-7376, NAS8-39747 and Lockheed Martin Independent Research

Funds, and was carried out while AMR held the Sir Norman Lockyer Fellowship, sponsored by the Royal Astronomical Society; AMR is also grateful for support from the Engineering and Physical Sciences Research Council.

APPENDIX A: NUMERICAL METHOD

We obtain solutions by separating the spatial operations from those required for integrating in time. We achieve sixth-order spatial accuracy using compact finite differences and fourth-order temporal accuracy using a modified Bulirsch–Stoer technique for integrating forward in time. Here we discuss the details of these methods and assess the accuracy of our implementation of them.

A1 Spatial Operators

Our compact difference formulation follows that of Lele (1992): the derivative f'_i of the function f_i at gridpoint i is evaluated by solving

$$\alpha f'_{i-1} + f'_i + \alpha f'_{i+1} = \frac{a}{\delta x}(f_{i+1} - f_{i-1}) + \frac{b}{\delta x}(f_{i+2} - f_{i-2}), \tag{A1}$$

where δx is the mesh interval, x represents r or z, $\alpha = 1/3$, $a = 7/9$ and $b = 1/36$. The second derivative f''_i is evaluated in an analogous manner with

$$\alpha f''_{i-1} + f''_i + \alpha f''_{i+1} = \frac{a}{\delta x^2}(f_{i+1} - 2f_i + f_{i-1}) + \frac{b}{\delta x^2}(f_{i+2} - 2f_i + f_{i-2}), \tag{A2}$$

where $\alpha = 2/11$, $a = 12/11$ and $b = 3/44$. Both these forms are sixth order accurate in δx and require the solution of a tridiagonal system to determine the value of f'_i or f''_i.

The boundaries for compact difference schemes are frequently evaluated using third-order accurate forms, which are sufficient for situations where the boundaries are relatively passive. However many, if not most problems in convection are controlled by the thermal and viscous boundary layers on the bounding surfaces. We therefore desire stable, higher-order boundary formulations. To prevent the integral properties of the solutions being dominated by boundary errors we have developed fifth order formulations. The convergence rate of the rms error for our complete spatial scheme are presented in Fig. 9(a). For Neumann boundary conditions the scheme remains 6th order accurate throughout the domain; for Dirichlet conditions the error is dominated by the 5th order boundary error. In both cases the error in computing the derivatives of the functions $\sin(2\pi x/\delta x\lambda)$ or $\cos(2\pi x/\delta x\lambda)$ drops to the numerical roundoff error in the vicinity of $\lambda = 10$. Our treatment of the second derivative boundary condition is fourth order on the boundaries for both choices of boundary conditions as seen in Fig. 9(b).

A2 Time Evolution

With the spatial accuracy of at least sixth order in the interior and at worst fourth order on the boundary, we now consider higher accuracy for integrating forward in time. One means of providing this is to use extrapolation techniques such as those of pioneered by Stoer and Bulirsch (1980) and developed by Deuflhard (1983). Alternatively, we could use a fourth-order Runge–Kutta method, but while the computational effort required is comparable, the extrapolation method is more flexible and more amenable to time dependent boundary conditions. Extrapolation methods can also be adapted to form a multirate method (Engstler and Lubich 1995) which can cope with some stiff systems that might otherwise require implicit schemes.

Our method advances the system, say $\boldsymbol{y}'(t) = \boldsymbol{f}(t, \boldsymbol{y})$ a fixed time step δt by making a series of successively more accurate preliminary advances $\delta t/n$ with successively smaller and more numerous steps n using a modified midpoint method. Given an initial $\boldsymbol{y}(t)$, we set

$$\boldsymbol{z}_1 = \boldsymbol{y}(t) + \frac{\delta t}{n}\boldsymbol{f}(t, \boldsymbol{y}) \tag{A3}$$

and compute

$$\boldsymbol{z}_{m+1} = \boldsymbol{z}_m + \frac{2\delta t}{n}\boldsymbol{f}(t + m\delta t/n, \boldsymbol{z}_m) \tag{A4}$$

for $m = 1, 2, \ldots, n-1$, to obtain

$$\boldsymbol{y}(t + \delta t) = \tfrac{1}{2}(\boldsymbol{z}_n + \boldsymbol{z}_{n-1}) + \frac{\delta t}{n}\boldsymbol{f}(t, \boldsymbol{z}_n). \tag{A5}$$

A simple polynomial extrapolation then uses these preliminary values $\boldsymbol{y}(t + \delta t)$ for an increasing number of steps n to extrapolate to an infinite number of infinitesimal steps. We use the standard sequence suggested by Press et al. (1986) with $n = 2, 4, 6, 8, 12$, corresponding to one, two, three, four and six modified-midpoint steps. For second-order accuracy two evaluations of the system of equations is required; for fourth-order, six; for sixth-order, twelve; etc. The penalty for such accuracy is the need for additional memory to store the temporary results. Unlike the standard Bulirsch–Stoer methods, our scheme specifies the formal accuracy desired prior to each step, which greatly reduces the memory requirements. For accuracies of $O(\delta t^4)$ and beyond the code requires the storage penalty of a factor of five (the working variables and four scratch arrays of equivalent size). The accuracy for the fourth-, sixth- and eighth-order integrators is displayed in Fig. 10(a) for the solution of a harmonic oscillator as functions of the sampling frequency ω. All three converge at the expected rate from the Nyquist frequency and reach machine roundoff error with ten samples per period. From Fig. 9(a) and Fig. 10(a), the accuracies of the spatial and temporal schemes have errors of about 0.1% for the same spatial/temporal sampling rate. This suggests that the relative error for solutions to the hyperbolic systems should be comparable for Courant numbers of unity. A simple test using the advection of an arctangent function of width χ is shown in Fig. 10(b), which supports this conjecture: the error is limited by the underlying fifth-order spatial resolution once the Courant number drops below unity.

A3 Comparison with previous work

Here we compare our scheme with others when applied to a particular problem. A good candidate for this is the oscillatory solution to the magnetoconvection problem in two-dimensional Cartesian geometry, originally discovered by Hurlburt & Toomre (1988), which was later found to arise in a nonlinear bifurcation from the steady solution branch (Weiss et al. 1990) and which has been verified with different

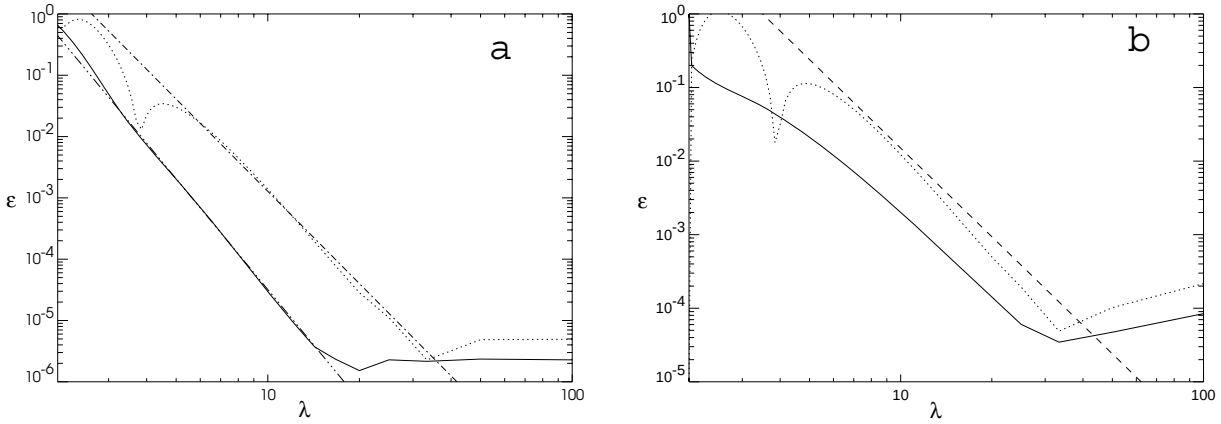

Figure 9. The global rms error ϵ for the complete compact difference scheme decreases with increasing wavelength λ as measured in units of the grid spacing δx. (a) The error of the first derivative for Neumann boundary conditions (solid), decreases as λ^6 (broken solid) from the Nyquist wavelength down to machine roundoff. The error for Dirichlet conditions (dotted) decreases as λ^5 (dot-dashed), due to the influence of fifth-order boundary conditions. (b) Errors for both boundary conditions decrease as λ^4 (dashed) in evaluating the second derivative.

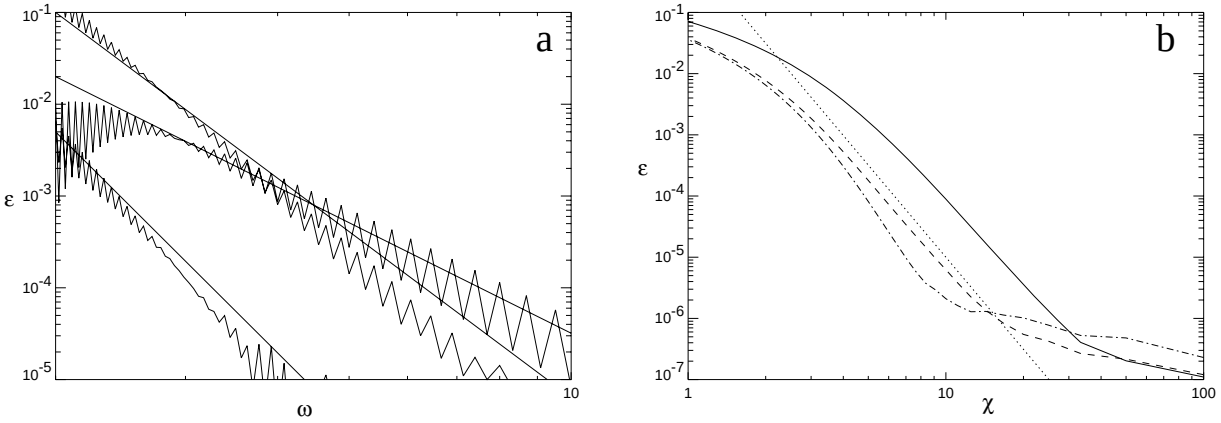

Figure 10. (a) The error ϵ at the end of 100 steps for the 4^{th}-, 6^{th}- and 8^{th}-order accurate Bulirsch–Stoer integrator applied to the harmonic oscillator decreases with increasing sampling frequency ω. (b) The rms error ϵ at the end of 0.6 time units versus the width χ of the advected arctangent function at unit velocity for three sizes of timestep. The error is largest for largest step $\delta t = 1.5\delta x$ (solid) and decreases down to the underlying accuracy of the spatial operators as the step size is reduced to $0.75\delta x$ (dashed) and $0.375\delta x$ (dot-dashed). For reference we include the dotted line which indicates a χ^5 relationship.

numerical methods and various combinations of boundary conditions (Hurlburt et al. 1996). This instability occurs in systems where the value of the magnetic Prandtl number $\zeta = \rho\zeta_0$ passes through unity within the domain. If $\zeta < 1$ everywhere then the initial bifurcation from the static state can be oscillatory. If $\zeta > 1$ then it is always steady. The mixed state is a nonlinear coupling between these solution branches. All previous solutions have been for periodic conditions in two-dimensional Cartesian geometry, and here we have impermeable, stress-free walls with axisymmetric geometry (we use the usual vertical magnetic field and constant temperature upper boundary conditions for this comparison). The geometric differences disappear if we take a cylindrical annulus of inner radius $\Gamma_{\rm i}$ and outer radius $\Gamma_{\rm o}$, with $\Gamma_{\rm o}/\Gamma_{\rm i} - 1 \ll 1$. Since the solutions possess two stationary, vertical symmetry planes, the difference in boundary conditions should be small. One such solution, with $\Gamma_{\rm i} = 100$ and $\Gamma_{\rm o} = \Gamma_{\rm i} + 4/3$, compares well with those found by Weiss et al. (1990). We have found that the bifurcation point for the oscillatory instability is $R \approx 43,500$, which is about two percent less than the value estimated by Weiss et al. (1990).

Comparison of the computational effort of the magnetoconvection code against previous schemes are quite favourable. The codes used by Hurlburt et al. (1996) typically required about 0.9 seconds of CPU time for each step $\delta t = 0.1\delta t_{\rm a}$. The code described above required 3.8 seconds of CPU time for each step on the same computer, but operates with a step size $\delta t = \delta t_{\rm a}$ for comparable geometry and parameters. The total computational effort to advance the solution one time unit using our more accurate method is thus reduced by more than a factor of two.

REFERENCES

Alexander, D., Hurlburt, N.E., Rucklidge, A.M., 2000, Proceedings of the SOHO 8 meeting (submitted)
Blanchflower, S.M., Rucklidge, A.M., Weiss, N.O., 1998, MNRAS, 301, 593
Cameron, R., 2000, Sol. Phys., (submitted)
Cattaneo, F., 1984a, PhD thesis, Cambridge
Cattaneo, F., 1984b, in Guyenne, T.D., Hunt, J.J., eds, The Hydromagnetics of the Sun. ESA SP-220, Noordwijkerhout, p. 47
Chandrasekhar, S., 1961, Hydrodynamic and Hydromagnetic Stability. Clarendon Press, Oxford
Deuflhard, P., 1983, Numer. Math., 41, 399
Duvall Jr, T.L., D'Silva, S., Jeffries, S.M., Harvey, J.W., Schou, J., 1996, Nat, 379, 235
Engstler, Ch., Lubich, Ch., 1997, Computing, 58, 173
Galloway, D.J., Moore, D.R., 1979, Geophys. Astrophys. Fluid Dyn., 12, 73
Galloway, D.J., Proctor, M.R.E., 1983, Geophys. Astrophys. Fluid Dyn., 24, 109
Galloway, D.J., Proctor, M.R.E., Weiss, N.O., 1978, J. Fluid Mech., 87, 243
Hughes, D.W., Falle, S.A.E.G., Joarder, P., 1998, MNRAS, 298, 433
Hurlburt, N.E., Toomre, J., 1988, ApJ, 327, 920
Hurlburt, N.E., Toomre, J., Massaguer, J.M., 1984, ApJ, 282, 557
Hurlburt, N.E., Proctor, M.R.E., Weiss, N.O., Brownjohn, D.P., 1989, J. Fluid Mech., 207, 587
Hurlburt, N.E., Matthews, P.C., Proctor, M.R.E., 1996, ApJ, 457, 933
Hurlburt, N.E., Matthews, P.C., Rucklidge, A.M., 2000, Sol. Phys., (submitted)
Jahn, K., Schmidt, H.U., 1994, A&A, 290, 295
Jones, C.A. & Galloway, D.J., 1993, J. Fluid Mech., 253, 297
Julien, K., Knobloch, E., Tobias, S.M., 2000, J. Fluid Mech., (submitted)
Keil, S.L., Balasubramaniam, K.S., Smaldone, L.A., Reger, B., 1999, ApJ, 510, 422
Landau, L.D., Lifshitz, E.M., 1987, Fluid Mechanics (2nd edition). Pergamon, Oxford
Leka, K.D., Skumanich, A., 1998, ApJ, 507, 454
Lele, S.K., 1992, J. Comput. Phys., 103, 16
Matthews, P.C., Hurlburt, N.E., Proctor, M.R.E., Brownjohn, D.P., 1992, J. Fluid Mech., 240, 559
Martens, P.C.H., Hurlburt, N.E., Title, A.M., Acton, L.W., 1996, ApJ, 463, 372
Meyer, F., Schmidt, H.U., Weiss, N.O., Wilson, P.R., 1974, MNRAS, 169, 35
Meyer, F., Schmidt, H.U., Weiss, N.O., 1977, MNRAS, 179, 741
Neukirch, T., Martens, P.C.H., 1998, A&A, 332, 1075
Nordlund, Å., Stein, R.F., 1997, in Pijpers, F.P., Christensen-Dalsgaard, J., Rosenthal, C.S., eds, Solar Convection, Oscillations and their Relationship. Kluwer, Dordrecht, p. 79
Parker, E.N., 1975, Sol. Phys., 40, 291
Parker, E.N., 1979, ApJ, 230, 905
Press, W.H., Flannery, B.P., Teukolsky, S.A., Vetterling, W.T., 1986, Numerical Recipes – the Art of Scientific Computing. Cambridge Univ. Press, Cambridge
Rast, M.P., 1995, ApJ, 443, 863
Rast, M.P., Fox, P.A., Lin, H., Lites, B.W., Meisner, R.W., White, O.R., 1999, Nat, 401, 678
Rimmele, T.R., 1995a, A&A, 298, 260
Rimmele, T.R., 1995b, ApJ, 445, 511
Rucklidge, A.M., Schmidt, H.U., Weiss, N.O., 1995, MNRAS, 273, 491
Rucklidge, A.M., Weiss, N.O., Brownjohn, D.P., Matthews, P.C., Proctor, M.R.E., 2000, J. Fluid Mech., (submitted)
Schlichenmaier, R., Jahn, K., Schmidt, H.U., 1998, A&A, 337, 897
Schlichenmaier, R., Schmidt, W., 1999, A&A, 349, L37
Shine, R.A., Title, A.M., Tarbell, T.D., Smith, K., Frank, Z.A., 1994, ApJ, 430, 413
Skumanich, A., 1999, ApJ, 512, 975
Sobotka, M., Brandt, P.N., Simon, G.W., 1997, A&A, 328, 689
Sobotka, M., Vázquez, M., Bonet, J.A., Hanslmeier, A., Hirzberger, J., 1999a, ApJ, 511, 436
Sobotka, M., Brandt, P.N., Simon, G.W., 1999b, A&A, 348, 621
Spruit, H.C., 1997, Mem. S. A. It., 68, 397
Spruit, H.C., Nordlund, Å., Title, A.M., 1990, ARA&A, 28, 263
Stanchfield II, D.C.H., Thomas, J.H., Lites, B.W., 1997, ApJ, 477, 485
Steffen, M., Ludwig, H.-G., Krüss, A., 1989, A&A, 213, 371
Stein, R.F., Nordlund, Å., 1989, ApJ, 342, L95
Stein, R.F., Nordlund, Å., 1998, ApJ, 499, 914
Steiner, O., Grossman-Doerth, U., Knölker, M., Schüssler, M., 1998, ApJ, 495, 468
Stoer, J., Bulirsch, R., 1980, Introduction to Numerical Analysis. Springer, New York
Sütterlin, P., Thim, F., Schröter, E.H., 1994, in Schüssler, M., Schmidt, W., eds, Solar Magnetic Fields. Cambridge Univ. Press, Cambridge, p. 213
Tao, L.L., Weiss, N.O., Brownjohn, D.P., Proctor , M.R.E., 1998, ApJ, 496, L39
Thomas, J.H., Weiss, N.O., 1992, in Thomas, J.H., Weiss, N.O., eds, Sunspots: Theory and Observations. Kluwer, Dordrecht, p. 3
Title, A.M., Frank, Z.A., Shine, R.A., Tarbell, T.D., Topka, K.P., Scharmer, G., Schmidt, W., 1993, ApJ, 403, 780
Tuckerman, L.S., Barkley, D., 1988, Phys. Rev. Lett., 61, 408
Watson, P.G., 1995, PhD thesis, Cambridge
Weiss, N.O., 1966, Proc. R. Soc. Lond. A, 293, 310
Weiss, N.O., Brownjohn, D.P., Hurlburt, N.E., Proctor, M.R.E., 1990, MNRAS, 245, 434
Weiss, N.O., Brownjohn, D.P., Matthews, P.C., Proctor, M.R.E., 1996, MNRAS, 283, 1153
Westendorp Plaza, C., del Toro Iniesta, J.C., Ruiz Cobo, B., Martinez Pillet, V., Lites, B.W., Skumanich, A., 1997, Nat, 389, 47

This paper has been produced using the Royal Astronomical Society/Blackwell Science TEX macros.